

Hyperspectral Mixed Noise Removal via Subspace Representation and Weighted Low-rank Tensor Regularization

Hang Zhou, Yanchi Su, Zhanshan Li

Abstract—Recently, the low-rank property of different components extracted from the image has been considered in many hyperspectral image denoising methods. However, these methods usually unfold the 3D tensor to 2D matrix or 1D vector to exploit the prior information, such as nonlocal spatial self-similarity (NSS) and global spectral correlation (GSC), which break the intrinsic structure correlation of hyperspectral image (HSI) and thus lead to poor restoration quality. In addition, most of them suffer from heavy computational burden issues due to the involvement of singular value decomposition operation on matrix and tensor in the original high-dimensionality space of HSI. We employ subspace representation and the weighted low-rank tensor regularization (SWLRTR) into the model to remove the mixed noise in the hyperspectral image. Specifically, to employ the GSC among spectral bands, the noisy HSI is projected into a low-dimensional subspace which simplified calculation. After that, a weighted low-rank tensor regularization term is introduced to characterize the priors in the reduced image subspace. Moreover, we design an algorithm based on alternating minimization to solve the nonconvex problem. Experiments on simulated and real datasets demonstrate that the SWLRTR method performs better than other hyperspectral denoising methods quantitatively and visually.

Index Terms—subspace representation, weighted low-rank tensor regularization, HSI denoising.

I. INTRODUCTION

THANKS to the advancements in imaging technology, hyperspectral image (HSI) is capable of providing abundant information regarding the wavelengths beyond the visible spectrum and have a wide range of applications including medical diagnosis [1], [2], [3], geothermal exploration [4], [5], [6], agriculture [7], [8], [9]. Unfortunately, different types of noise including stripes, deadlines, impulse noise, and Gaussian noise will be inevitably introduced in the hyperspectral imaging process, which considerably damages the image quality and limits further applications including image classification [10], [11] and target detection [12], [13]. Therefore, image denoising, as a preprocessing step in many computer vision tasks, is an essential and significant research topic.

During the past few decades, researches on hyperspectral images denoising has extensively proved that spatial nonlocal self-similarity and global spectral correlation are important

prior information. A derivative-domain wavelet transform model is designed by Othman and Qian [14] resorted to the signal regular dissimilarity along spatial and the spectral domain, which made an initial attempt to consider both priors. Subsequently, numerous denoising methods come up to benefit from the spatial and spectral features of HSIs. For example, a sparse representation model was developed by Qian et al. [15] to utilize the two priors of HSI. Under a unified probabilistic framework, Zhong and Wang [16] considered spatial and spectral correlations and designed a multiple spectral-band conditional random field (MSB-CRF) method. A total variation model [17] is proposed by Yuan et al. which adaptively adjust the denoising ability concerning the spatial property and noise intensity in each spectral band. To sum up, many advanced denoising techniques employed spectral and spatial information of the HSIs, including wavelet shrinkage [14], [18], [19], sparse representation [15], [20], etc.

For hyperspectral images, spectrally adjacent bands typically exhibit strong correlations due to the similar exposure time and wavelength, which reveals the low-rank property of hyperspectral images in the spectral domain. To explore the spectral low rankness, Zhang et al. [21] split HSI into many overlapping full-band 3D cubes, then unfolded the 3D cubes to a matrix along with the spectral mode, and denoised under a low-rank matrix recovery (LRMR) [22] framework. After that, they proposed a low-rank matrix approximation (LRMA) model [23] to accommodate the differences in noise intensity at different bands which significantly enhance the denoising performance of LRMR. Based on LRMA, other approximation or relaxation of matrix rank were also proposed and integrated into the denoising model, such as γ -norm [24] and weighted Schatten p -norm [25] etc. Follow this line, W. He et al. [26] employed low-rank matrix factorization (LRMF) to capture the spectral correlations as well as reduce the algorithm complexity. These low-rank-based methods have achieved comparable results for exploring the global spectral correlation, however, the solving process always containing singular value decomposition, which brings heavy computational burden when operated on high-dimensional data.

The spatial nonlocal self-similarity means that for any image patch extracted from a hyperspectral image, several patches similar to the reference patch can be found in the HSI, which suggests that the matrix generated by vectorizing each band of grouped similar patches as the column has a strong correlation can and is low-rank. Wang et al. [27] grouped the similar patches and explored the nonlocal self-similarity on a

Hang Zhou is with the Department of Software Engineering, Jilin University, Changchun (e-mail: zhouhang19970714@163.com).

Yanchi Su is with the Department of Artificial Intelligence, Jilin University, Changchun (e-mail: suyanchi@gmail.com).

Zhanshan Li is with the Department of Software Engineering, Jilin University, Changchun (e-mail: zslzsl@163.com). Corresponding author.

reconstructed group. Later, Xue et al. [28] performed a low-rank regularized method on the similar patches in each cluster to characterize the spatial structure. Common operations of the above low-rank matrix-based methods are constructing a low-rank component according to clean HSI priors and explore its low-dimensional structure, which destroys the intrinsic structure of 3-D cube/image and has room for further improvement. Besides, the block matching process on high-dimensional data is a time-consuming operation.

In order to characterize the intrinsic structure of HSIs, many methods employed a low-rank tensor-based model and obtain better denoising performance. Tucker decomposition and CANDECOMP/PARAFAC (CP) decomposition are two typical tensor decomposition methods. Based on CP decomposition, Liu et al. [29] used parallel factor analysis (PARAFAC) model for HSI denoising and estimated the optimal rank of PARAFAC by calculating the covariance matrix after unfolding the matrix along n -mode. A new criterion is defined by Guo et al. [15] to select the optimal CP rank, which calculates the minimum number of rank-1 tensors needed to describe a tensor. However, the prior information has not been fully taken into account as these methods concern HSI as a whole and ignore the information in other data structures, which usually results in suboptimal denoising performance. Based on Tucker decomposition, the ISTReg [30] proposed a tensor sparsity measure composed of the core tensor and rank of matrix unfolded along with three modes, which makes the large computation problem more serious. Chang et al. [31] designed a weighted low-rank tensor recovery model applied on denoising and other visual tasks, where the singular values obtained by Tucker decomposition are treated differently concerning its contribution to rebuilding the original image. By formulating the denoising process as a low-rank tensor recovery (LRTR) problem, Fan et al. introduced a new tensor singular value decomposition (t-SVD) method [32]. [33] and [34] combined Tucker decomposition and total variation method to describe the global correlation and local similarity within a patch. It is worth mentioning that Chang et al. [35] analyzed the low-rank characteristics in matrices and tensors and explained why the tensor-based method is better than the matrix-based method. Therefore, the tensor-based denoising method is an effective way to make full use of the global spectral correlation (GSC), nonlocal self-similarity (NSS) over space as well as maintaining the inherent structure, while at the expense of high complexity.

As for reducing the computational complexity, subspace-based [36] HSI denoising methods are effective techniques, which projects HSIs to eigen images based on high correlation existing among spectrum. Zhuang and Bioucas-Dias [37] made a first try to explore the global spectral correlation by subspace representation, which reconstructed similar 3D patches from the representation coefficients image to a low-rank tensor and employed low-rank tensor factorization to remove noise. After that, also in the framework of subspace representation, they proposed a fast hyperspectral denoising (FastHyDe) algorithm for Gaussian and Poissonian noise [38]. Sun et al. [39] made the first attempt to remove HSI mixed noise based on subspace representation, and the superpixel segmentation is employed

to exploit the spatial low rankness. He et al. [40] presented an integrated paradigm based on subspace representation and introduced an iterative mechanism on subspace. In addition, Cao et al [41] introduced nonlocal low-rank factorization on spatial domain of the subspace. In the above methods, the low rankness of the spectrum is characterized by subspace representation, and the subspace-based denoising method is capable of reducing complexity significantly.

As we know, real-world HSIs usually disturbed by Gaussian noise and different types of sparse noise due to the uncertainties during image acquisition process. Motivated by [31] and [41], we propose a method to remove mixed noise in hyperspectral image by combining subspace representation with weighted low-rank tensor regularization. On the one hand, the subspace representation allows the method to impose the spectral correlation and convert the problem into an estimate of the subspace coefficients, thus simplifying the calculation. On the other hand, the introduced weighted low-rank tensor regularization term characterize the priors in the reduced image effectively, where the singular value of the core tensor is punished according to its importance for recovering real HSI. The contributions of our work are summarized as follow:

- 1) We designed a novel mixed noise removal model for hyperspectral images. Based on the high spectral correlation, the subspace representation decomposes the noisy hyperspectral image into a mode-3 tensor-matrix product, which simplifies the estimation of clean images. We reconstruct the similar patches groups searched from reduced image to obtain a tensor with low rankness, and introduce a weighted low-rank tensor regularization term to constrain the low-rank characteristics considering the physical meaning of core tensor. In addition, the sparse noise constrained by l_1 -norm is also integrated into the model to remove the sparse noise. In the denoising process, the intrinsic structure of the tensor is better preserved and the computational complexity is lower than comparison algorithms.
- 2) An alternating minimization-based algorithm is designed to solve the proposed denoising model and it is possible to obtain an optimal solution.
- 3) Furthermore, simulated and real datasets experiments prove that our method is superior to existing methods both quantitatively and qualitatively.

II. NOTATIONS AND PRELIMINARIES

In this article, the tensor is denoted by capitalized calligraphic letter, i.e. \mathcal{X} ; matrix by uppercase letter, i.e. X ; vector by lowercase letter, i.e. x . The i -th entry of vectors x is represented as x_i , the element in the i -th row and j -th column of the matrices X is expressed as X_{ij} , the element (i, j, k) of tensors \mathcal{X} is expressed as x_{ijk} . The Frobenius norm of a N order tensor $\mathcal{X} \in \mathbb{R}^{I_1 \times I_2 \times \dots \times I_N}$ is defined as $\|\mathcal{X}\|_F = \left(\sum_{i_1=1}^{I_1} \sum_{i_2=1}^{I_2} \dots \sum_{i_N=1}^{I_N} |x_{i_1 i_2 \dots i_N}|^2 \right)^{1/2}$, its l_1 norm is defined

as $\|\mathcal{X}\|_1 = \sum_{i_1=1}^{I_1} \sum_{i_2=1}^{I_2} \cdots \sum_{i_N=1}^{I_N} |x_{i_1 i_2 \cdots i_N}|$. The mode- n vector of a N -order tensor $\mathcal{X} \in \mathbb{R}^{I_1 \times I_2 \times \cdots \times I_N}$ is an I_n dimensional vector with i_n as the element subscript variable, and all other subscripts $\{i_1, \cdots, i_N\} \setminus i_n$ are fixed, denoted as $X_{i_1 \cdots i_{n-1} i_{n+1} \cdots i_N}$. The matrixization of a tensor refers to the transformation of reorganizing an N -order tensor into a matrix form, including horizontal expansion and vertical expansion. The mode- n vectors of the N -order tensor $\mathcal{X} \in \mathbb{R}^{I_1 \times I_2 \times \cdots \times I_N}$ arranged in the horizontal direction called mode- n unfolding along the horizontal, expressed as $X_{(n)}, X_{(n)} \in \mathbb{R}^{(I_1 \cdots I_{n-1} I_{n+1} \cdots I_N) \times I_n}$. The mode- n vectors of the tensor arranged in the vertical direction called mode- n unfolding along the vertical, denoted as $X^{(n)}, X^{(n)} \in \mathbb{R}^{(I_1 \cdots I_{n-1} I_{n+1} \cdots I_N) \times I_n}$. The mode- n tensor-matrix product of a N -order tensor $\mathcal{X} \in \mathbb{R}^{I_1 \times I_2 \times \cdots \times I_N}$ and a $J_n \times I_n$ matrix U is represented by $\mathcal{X} \times_n U$, which is a $I_1 \cdots I_{n-1} \times J_n \times I_{n+1} \cdots I_N$ tensor, its elements are defined as $(\mathcal{X} \times_n U)_{i_1 \cdots i_{n-1} j_{n+1} \cdots i_N} \stackrel{def}{=} \sum_{i_n=1}^{I_n} x_{i_1 i_2 \cdots i_N} u_{j_n i_n}$, $j = 1, \cdots, J_n, i_k = 1, \cdots, I_k, k = 1, \cdots, N$. Tucker decomposition is a kind of high-order singular value decomposition that each $I_1 \times I_2 \times \cdots \times I_N$ tensor \mathcal{X} can be decomposed into a mode- n product $\mathcal{X} = \mathcal{G} \times_1 U^{(1)} \times_2 U^{(2)} \cdots \times_N U^{(N)}$, where $U^{(n)}$ is a semi-orthogonal $I_n \times J_n$ matrix, the core tensor $\mathcal{G} \in \mathbb{R}^{J_1 \times J_2 \times \cdots \times J_N}$ is generally a full tensor, representing the interaction among each modes of matrices $U^{(n)}, n = 1, \dots, N$. Besides, the kronecker product of $m \times n$ matrix $A = [a_1, \cdots, a_n]$ and $p \times q$ matrix B is denoted as $A \otimes B = [a_1 B, \cdots, a_n B] = [a_{ij} B]_{i=1, j=1}^{m, n}$, which is a matrix of size $mp \times nq$.

III. PROBLEM FORMULATION

A. Problem formulation

The noisy hyperspectral image $\mathcal{Y} \in \mathbb{R}^{n_1 \times n_2 \times n_3}$ is assumed to be the sum of clean signal \mathcal{X} and noise, where n_1, n_2 are the length and width of hyperspectral image, and n_3 is the number of spectral bands. The noise is modeled as random noise \mathcal{N} and sparse noise \mathcal{S} according to the characteristics of the noise intensity distribution. Therefore, the degradation model of removing HSI mixed noise can be expressed as

$$\mathcal{Y} = \mathcal{X} + \mathcal{N} + \mathcal{S} \quad (1)$$

The purpose of hyperspectral image denoising is to recover clean signal \mathcal{X} from the observed image \mathcal{Y} , which is a difficult ill-posed problem. The key to solving this problem is to establish appropriate regularization based on reasonable HSI prior. On this basis, the denoising model of the hyperspectral image can be expressed as

$$\{\hat{\mathcal{X}}, \hat{\mathcal{S}}\} = \arg \min_{\mathcal{X}, \mathcal{S}} \frac{1}{2} \|\mathcal{Y} - \mathcal{X} - \mathcal{S}\|_F^2 + \lambda_1 J_1(\mathcal{X}) + \lambda_2 J_2(\mathcal{S}) \quad (2)$$

where $\|\cdot\|_F^2$ denotes the Frobenius norm of a tensor and measures the error bounds between the reconstructed image and noisy HSI. $J_1(\mathcal{X})$ and $J_2(\mathcal{S})$ are the regularization terms of the clean image \mathcal{X} and sparse noise \mathcal{S} , respectively. λ_1 and λ_2 are the parameters to balance the data fidelity term and the regularization term. Here, the sparsity of \mathcal{S} is constraint by l_1 norm. So (2) can be converted to:

$$\{\hat{\mathcal{X}}, \hat{\mathcal{S}}\} = \arg \min_{\mathcal{X}, \mathcal{S}} \frac{1}{2} \|\mathcal{Y} - \mathcal{X} - \mathcal{S}\|_F^2 + \lambda_1 J_1(\mathcal{X}) + \lambda_2 \|\mathcal{S}\|_1 \quad (3)$$

B. Subspace representation

Due to the high correlation in spectral, the combination of a few pure endmembers can express any spectral signature linearly. Assuming that HSI \mathcal{X} is located in a k -dimensional spectral subspace \mathcal{H}_k , the clean hyperspectral image \mathcal{X} can be expressed as $\mathcal{X} = \mathcal{Z} \times_3 A$, where $A \in \mathbb{R}^{n_3 \times k}$ is an orthogonal matrix holding the basis of the reduced image $\mathcal{Z} \in \mathbb{R}^{n_1 \times n_2 \times k}$. Therefore, HSI denoising model (3) can be reformulated as follows:

$$\{\hat{A}, \hat{\mathcal{Z}}, \hat{\mathcal{S}}\} = \arg \min_{\mathcal{X}, \mathcal{S}} \frac{1}{2} \|\mathcal{Y} - \mathcal{Z} \times_3 A - \mathcal{S}\|_F^2 + \lambda_1 J_1(\mathcal{Z}) + \lambda_2 \|\mathcal{S}\|_1 \quad s.t. AA^T = I_k \quad (4)$$

W. He et al. [42] has proved that the orthogonal constraint help to exclude noise from A and maintain the distribution of noise in the reduced image. Besides, the benefits of factorizing the HSI to a mode-3 tensor-matrix product include preserving the integrity of the structural information and reducing the computational cost significantly.

C. Weighted low-rank tensor regularization

In the last decades, nonlocal similar patch-based methods have demonstrated that grouping similar patches do enhance the low-rank nature. Therefore, we exploit the two inherent priors of the reduced image to obtain a tensor with a more significant low-rank property by aggregating the similar full-band patches, which benefits the HSI image denoising. In practical applications, 3-D patches similar to reference 3-D patches are searched in adjacent areas. Define that patch size is $p \times p \times k$, and the number of similar patches is q . The process of constructing low-rank tensor \mathcal{Z}_i from \mathcal{Z} is as follows:

- 1) Searching: patches are sampled in the neighborhood, and most of the pixels appeared in several patches.
- 2) Block matching: calculate the euclidean distance between the reference image patch and the selected patches, then retain the first q patches that more similar to the reference image.
- 3) Unfolding: reshape each 3-D image patch in the group into a $p^2 \times k$ matrix to get the mode-3 vectors of these patches.
- 4) Stacking: stack the q mode-3 vectors obtained in step 3) into a tensor of size $p^2 \times q \times k$, denoted as \mathcal{Z}_i .

The above process is described as $\mathcal{Z}_i = \mathfrak{R}_i \mathcal{Z}$, where i is the top-left corner pixel coordinates, and \mathfrak{R}_i represents a series of operations extracting the low-rank tensor \mathcal{Z}_i from the reduced image \mathcal{Z} .

The different performances of [32], [33], [34] are caused by the different regularization term used for the low-rank tensor, falling into this line, we introduce a low-rank tensor regularization term [31] to exploit the prior knowledge of \mathcal{Z}_i while preserving intrinsic structure. Therefore, estimating the corresponding low-rank approximation, i.e. clean tensor \mathcal{L}_i from \mathcal{Z}_i can be written as:

$$\hat{\mathcal{L}}_i = \arg \min_{\mathcal{L}_i} \frac{1}{2} \|\mathcal{Z}_i - \mathcal{L}_i\|_F^2 + \|\mathcal{L}_i\|_{w,*} \quad (5)$$

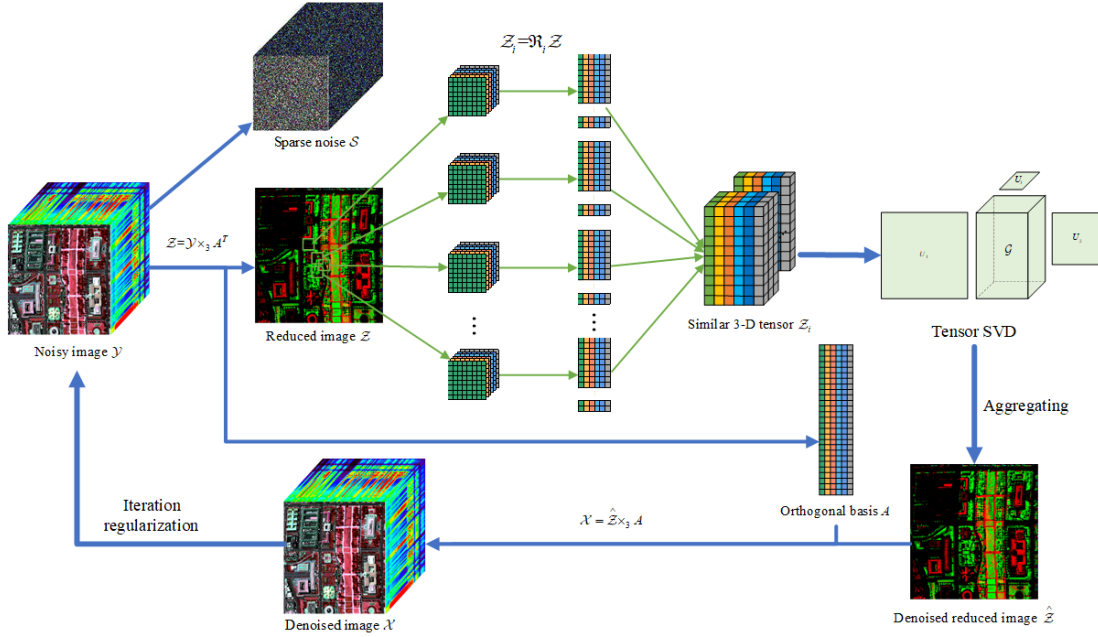


Fig. 1. The denoising process of proposed method. It includes subspace representation $\mathcal{Z} = \mathcal{Y} \times_y A^T$, block matching $\mathcal{Z}_i = \mathfrak{R}_i \mathcal{Z}$, Tensor SVD and iteration regularization, etc.

where $\|\mathcal{L}_i\|_{w,*} = \sum_j |w_j \sigma_j(\mathcal{L}_i)|_1$, $w = [w_1, \dots, w_n]$, w_j are the non-negative weights assigned to $\sigma_j(\mathcal{L}_i)$, and σ_i^2 is the noise variance.

In general, the singular values in the core tensors are mostly close to zero due to the strong correlation among \mathcal{Z}_i . Large singular values represent the energy of the major components of \mathcal{Z}_i , while small singular values tend to be larger than clean tensor due to noise interference. Therefore, it is rational to impose less penalty for larger singular values and more penalty for smaller singular values. A natural approach is that the value of weight assigned to $\sigma_j(\mathcal{L}_i)$ is inversely proportional to \mathcal{L}_i . According to WLTR [31], we set

$$w_j = c \sqrt{q} / (|\sigma_j(\mathcal{L}_i)| + \varepsilon) \quad (6)$$

where ε is a small constant that avoids being divided by zero, and $c > 0$ is a constant.

IV. DENOISING MODEL AND OPTIMIZATION ALGORITHM

A. Denoising model and optimization algorithm

By integrating the weighted low-rank tensor regularization with the framework of subspace representation, the HSI mixed noise removal model is proposed as

$$\begin{aligned} \{\hat{A}, \hat{\mathcal{Z}}, \hat{\mathcal{L}}_i, \hat{\mathcal{S}}\} = \arg \min_{A, \mathcal{Z}, \mathcal{L}_i, \mathcal{S}} & \frac{1}{2} \|\mathcal{Y} - \mathcal{Z} \times_3 A - \mathcal{S}\|_F^2 \\ & + \lambda_1 \sum_i \left(\frac{1}{\sigma_i^2} \|\mathfrak{R}_i \mathcal{Z} - \mathcal{L}_i\|_F^2 + \|\mathcal{L}_i\|_{w,*} \right) \\ & + \lambda_2 \|\mathcal{S}\|_1 \quad \text{s.t. } AA^T = I_k \end{aligned} \quad (7)$$

We introduce an algorithm based on an alternating minimization strategy to optimize the proposed model efficiently. The solution procedure of the model (7) mainly includes two steps: solving the low-rank tensor regularization term and the reduced image \mathcal{Z} .

1) *low-rank tensor regularization term*: In this subproblem, we need to estimate \mathcal{L}_i from the low-rank tensor \mathcal{Z}_i . By ignoring the variables irrelevant to \mathcal{L}_i in (7), we can get the subproblem:

$$\hat{\mathcal{L}}_i = \arg \min_{\mathcal{L}_i} \frac{1}{\sigma_i^2} \|\mathcal{Z}_i - \mathcal{L}_i\|_F^2 + \|\mathcal{L}_i\|_{w,*} \quad (8)$$

[31] developed an alternating direction minimization method for solving the problem (8). By replacing \mathcal{L}_i with the corresponding Tucker decomposition, the optimization problem shown in (8) is equivalent to the following problem:

$$\begin{aligned} \{\hat{\mathcal{G}}_i, \hat{U}_1, \hat{U}_2, \hat{U}_3\} = \arg \min_{\mathcal{G}_i, U_1, U_2, U_3} & \|\mathcal{Z}_i - \mathcal{G}_i \times_1 U_1 \times_2 U_2 \times_3 U_3\|_F^2 \\ & + \sigma_i^2 \|\mathcal{G}_i\|_1 \quad \text{s.t. } U_j^T U_j = I, j = 1, 2, 3 \end{aligned} \quad (9)$$

where j represents the mode index of a 3-order tensor, and \circ denotes the element-wise multiplication. To estimate U_1, U_2, U_3 iteratively, let $W_1 = \mathcal{Z}_{i(1)}(U_3 \otimes U_2)$, where \otimes denotes the Kronecker product, then

$$U_1 = PQ^T \quad (10)$$

where $W_1 = P\Sigma Q^T$ is the singular value decomposition of W_1 . By assuming $W_2 = \mathcal{Z}_{i(2)}(U_3 \otimes U_1)$, $W_3 = \mathcal{Z}_{i(3)}(U_2 \otimes U_1)$, U_2 and U_3 can be optimized by the similar procedures, respectively. Let $O_i = \mathcal{Z}_i \times_1 U_1^T \times_2 U_2^T \times_3 U_3^T$, \mathcal{G}_i can be obtained through

$$\mathcal{G}_i = \text{sign}(O_i) \max(|O_i| - w_i \sigma_i^2 / 2, 0) \quad (11)$$

After obtained four variables, the mode-3 tensor-matrix multiplication is performed to restored optimal \mathcal{L}_i .

Algorithm 1 SWLRTR for hyperspectral image denoising

Input: \mathcal{Y} : noisy hyperspectral image; k : subspace dimension;
 p : image patch size; q : number of non-local similar patches;

Output: Denoised image \mathcal{X}

```

1: Initialize:  $\mathcal{X}^1 = \mathcal{Y}^1 = \mathcal{Y}$ ,  $\mathcal{S} = 0$ ;
2: for  $n = 1, 2, 3 \dots N$  do
3:   Estimate orthogonal basis matrix  $A^n$  by Hysime [36];
4:   Compute the reduced image  $\mathcal{Z}^n$  according to  $\mathcal{Z}^n = \mathcal{Y}^n \times_3 A^n$ ;
5:   for each patch  $\mathcal{Z}_i^n$  in  $\mathcal{Z}^n$  do
6:     Find similar 3-D patch group to form tensor  $\mathcal{Z}_i$ ;
7:     for (low-rank tensor recovery)  $n_0 = 1 \dots N_0$  do
8:       Estimate weight vector  $w$  via Eq.(6);
9:       Estimate  $U_j$  via Eq.(10);
10:      Estimate the core tensor  $\mathcal{G}_i$  via Eq.(11);
11:      Get the Estimation  $\hat{\mathcal{L}}_i = \mathcal{G}_i \times_1 U_1 \times_2 U_2 \times_3 U_3$ ;
12:    end for
13:  end for
14:  Aggregate  $\hat{\mathcal{L}}_i$  to form  $\hat{\mathcal{Z}}^n$ ;
15:  repeat
16:    update  $\mathcal{S}$  via Eq. (14);
17:    update  $\mathcal{Z}^n$  via Eq.(16);
18:    update  $A^n$  via Eq.(18);
19:  until convergence
20:  Compute denoised  $\mathcal{X}^n$  according to  $\mathcal{X}^n = \mathcal{Z}^n \times_3 A^n$ ;
21:  Iterative regularization  $\mathcal{Y}^{n+1} = \alpha \mathcal{X}^n + (1 - \alpha) \mathcal{Y}$ 
22:   $k = k + \beta \times n$ 
23: end for
    
```

2) *the reduced image \mathcal{Z}* : With \mathcal{L}_i fixed, the formulation (7) is converted to the following minimization problem:

$$\begin{aligned} \{\hat{A}, \hat{\mathcal{Z}}, \hat{\mathcal{S}}\} = \arg \min_{A, \mathcal{Z}, \mathcal{S}} \frac{1}{2} \|\mathcal{Y} - \mathcal{Z} \times_3 A - \mathcal{S}\|_F^2 + \lambda_2 \|\mathcal{S}\|_1 \\ + \lambda_1 \sum_i \frac{1}{\sigma_i^2} \|\mathfrak{R}_i \mathcal{Z} - \mathcal{L}_i\|_F^2 \quad \text{s.t.} \quad AA^T = I_k \end{aligned} \quad (12)$$

The augmented lagrangian function of the subproblem (12) is

$$\begin{aligned} \{\hat{A}, \hat{\mathcal{Z}}, \hat{\mathcal{S}}\} = \arg \min_{A, \mathcal{Z}, \mathcal{S}} \frac{1}{2} \|\mathcal{Y} - \mathcal{Z} \times_3 A - \mathcal{S}\|_F^2 + \lambda_2 \|\mathcal{S}\|_1 \\ + \lambda_1 \sum_i \frac{1}{\sigma_i^2} \|\mathfrak{R}_i \mathcal{Z} - \mathcal{L}_i\|_F^2 + \xi_{(I_k)}(AA^T) \end{aligned} \quad (13)$$

where $\xi_{(I_k)}(\cdot)$ is the indicator function. To solve (13), we can alternately update \mathcal{S} , \mathcal{Z} , A :

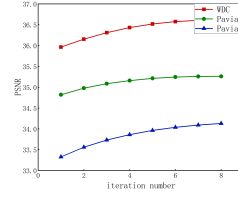
- Update \mathcal{S} : By fixing \mathcal{Z} and A , (13) can be written as

$$\hat{\mathcal{S}} = \arg \min_{\mathcal{S}} \frac{1}{2} \|\mathcal{Y} - \mathcal{Z} \times_3 A - \mathcal{S}\|_F^2 + \lambda_2 \|\mathcal{S}\|_1 \quad (14)$$

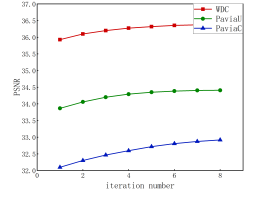
Its closed-form solution is $S_{\lambda_2}(\mathcal{Y} - \mathcal{Z} \times_3 A)$, where $S_{\omega}(x) = \text{sgn}(x) \max(|x| - \omega, 0)$ is the soft threshold operation.

- Update \mathcal{Z} : By fixing \mathcal{S} and A , (13) can be written as

$$\begin{aligned} \hat{\mathcal{Z}} = \arg \min_{\mathcal{Z}} \frac{1}{2} \|\mathcal{Y} - \mathcal{Z} \times_3 A - \mathcal{S}\|_F^2 \\ + \lambda_1 \sum_i \frac{1}{\sigma_i^2} \|\mathfrak{R}_i \mathcal{Z} - \mathcal{L}_i\|_F^2 \end{aligned} \quad (15)$$



(a) Gaussian+impulse



(b) Gaussian+impulse+deadlines

Fig. 2. PSNR values with the increase of iteration

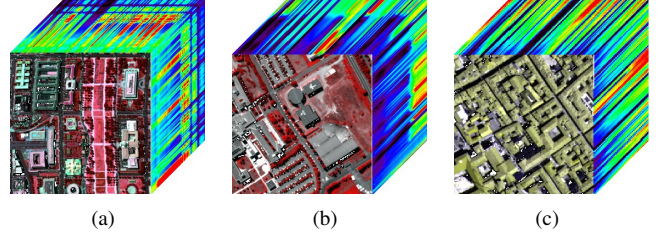


Fig. 3. (a) Washington DC Mall dataset (R:121,G:30,B:49) (b) Pavia University dataset (R:75,G:58,B:60) (c) Pavia Center dataset (R:24,G:30,B:6)

Equation (15) is a quadratic optimization problem and has a closed-form solution:

$$\begin{aligned} \hat{\mathcal{Z}} = \left(\mathbf{I}_k + \lambda_1 \sum_i \frac{2}{\sigma_i^2} \mathfrak{R}_i^T \mathfrak{R}_i \right)^{-1} \\ \times \left((\mathcal{Y} - \mathcal{S}) \times_3 A^T + \lambda_1 \sum_i \frac{2}{\sigma_i^2} \mathfrak{R}_i^T \mathcal{L}_i \right) \end{aligned} \quad (16)$$

- Update A : By fixing \mathcal{S} and \mathcal{Z} , (13) can be written as

$$\hat{A} = \arg \min_{A, AA^T = I_k} \frac{1}{2} \|\mathcal{Y} - \mathcal{Z} \times_3 A - \mathcal{S}\|_F^2 \quad (17)$$

Let $M = (\mathcal{Y} - \mathcal{S})^{(3)} \mathcal{Z}_{(3)}$, $M = U\Lambda V^T$ is assumed to be the singular value decomposition of M , then

$$\hat{A} = UV^T \quad (18)$$

B. Iterative regularization

Iterative regularization adds a specific proportion of the noise signal to the input of each iteration as a disturbance to the result. This strategy has been widely used to improve denoising performance. The formulation of updating the noisy image in the next iteration is

$$\mathcal{Y}_{n+1} = \alpha \mathcal{X}_n + (1 - \alpha) \mathcal{Y} \quad (19)$$

where α is a trade-off parameter that balances input in the next iteration, n is the number of iterations. Subspace size k is related to different datasets and noise intensity, we initialize k according to HySime [36]. The noise intensity of each iteration becomes weaker as the denoising process goes on, the denoised image is closer to the real image. Fig.2 presents the PSNR values on different noise types and datasets with the increase of iteration, proves that k should be gradually

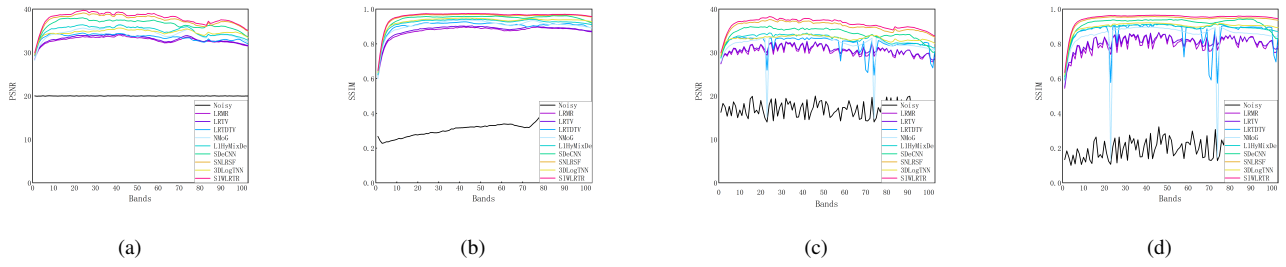


Fig. 4. PSNR and SSIM values of each band for PaviaU dataset in CASE1 and CASE2.(a) and (b) Case1. (c) and (d) Case2.

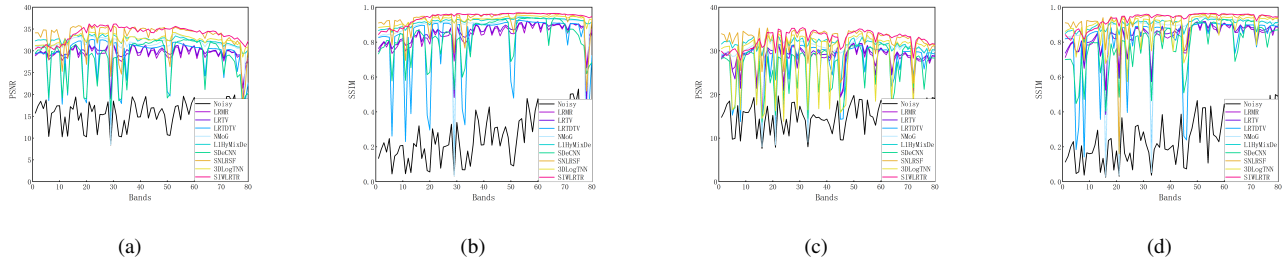


Fig. 5. PSNR and SSIM values of each band for PaviaC dataset in CASE3 and CASE4.(a) and (b) Case3. (c) and (d) Case4.

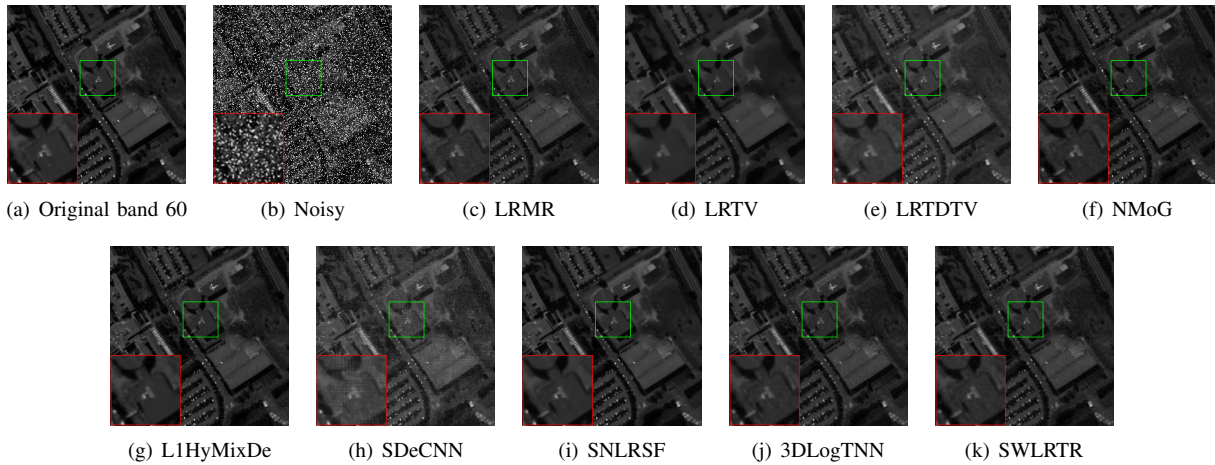


Fig. 6. Denoising results for PaviaU in CASE3.

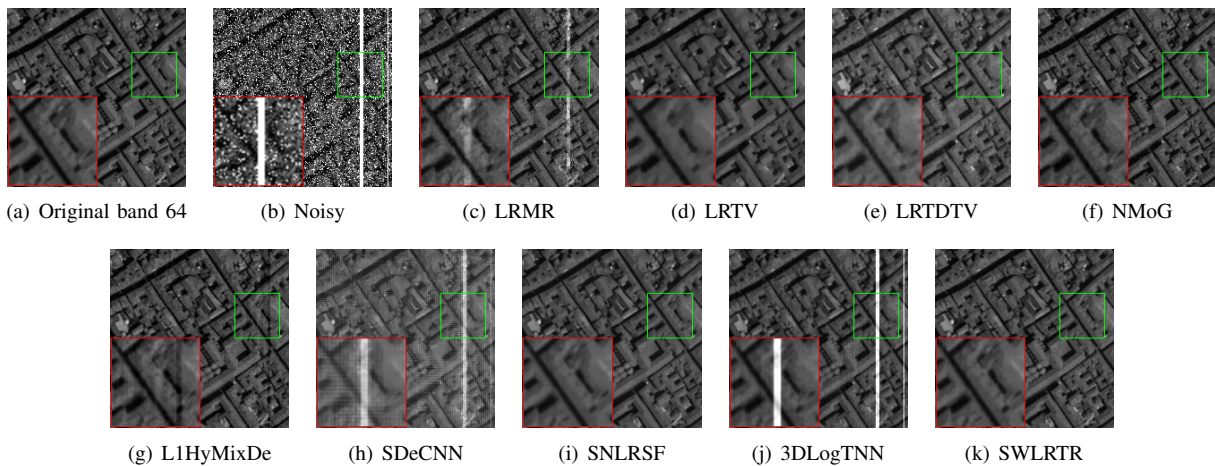


Fig. 7. Denoising results of PaviaC in CASE4.

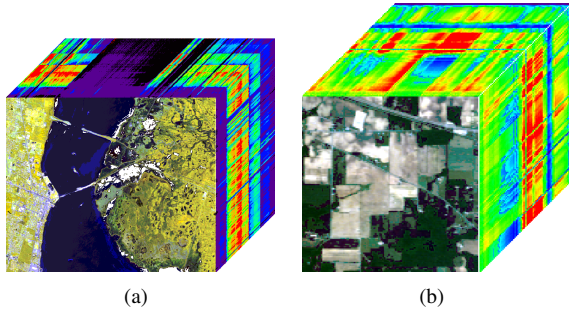


Fig. 8. (a) Kennedy Space Center dataset (R:50,G:77,B:29) (b) Indian Pines (R:29,G:19,B:9)

increased with the denoising process to retains more clean image information. Thus, k is updated by

$$k = k + \beta \times n \quad (20)$$

where β is a constant that determines the step size. In this way, A_{n+1} can extract more valuable information from the input image. The algorithm applied to solve the SWLRTR model is summarized as Algorithm 1, and the corresponding flowchart is shown as Fig.1.

C. Complexity analysis

In our algorithm, tucker decomposition and matrix multiplications operation dominate the computational complexity of SWLRTR. As for estimating \mathcal{Z}_i of size $p^2 \times k \times q$, it needs $N_0 \times k \times \mathcal{O}(\min(p^2k^2q^2, p^4kq))$ flops, where N_0 represents the number of iterations in low-rank tensor recovery. Hence, the process of obtain \mathcal{Z} costs $np \times N_0 \times k \times \mathcal{O}(\min(p^2k^2q^2, p^4kq))$, where np denotes the total number of patches search from HSI. After that, an amount of $kn_1n_2n_3$ and $\mathcal{O}(\min(n_3k^2, n_3^2k))$ flops are required to calculate \mathcal{S} and A each update, respectively. The overall computational complexity of SWLRTR is $N \times (np \times N_0 \times k \times \mathcal{O}(\min(p^2k^2q^2, p^4kq)) + N_1(kn_1n_2n_3 + \mathcal{O}(\min(n_3k^2, n_3^2k))))$, where N_1 is the number of iterations needed for convergence when estimate \mathcal{S} , \mathcal{Z} and A , N defines total number of iterations for denoising.

V. EXPERIMENTAL RESULTS

We design simulated and real-data experiments to verify the strong capability of SWLRTR on removing mixed noise. In the experiment, we chose LRMR [21], LRTV [26], LRTDTV [33], NMoG [24], L1HyMixDe [43], SDeCNN [44], 3DLogTNN [45], SNLRSF [41] as the comparison algorithms. All parameters are manually adjusted as recommended or according to the rules in the relevant literature to ensure optimal performance. For the convenience of calculation, we normalize the pixel values of HSI into [0,1]. The experiments are conducted in MATLAB R2018a using a 3.20-GHz CPU with 16-GB RAM.

A. Simulated data experiments

There are three HSI datasets adopted for simulated experiments, includes the Washington DC Mall, the Pavia University (PaviaU), and Pavia Center (PaviaC) datasets. The Washington

DC Mall data contains 1208×307 pixels and 191 spectral channels, where a subimage of size $256 \times 256 \times 191$ is used in our experiments. The subimages of Pavia University (PaviaU) and Pavia Center (PaviaC) datasets are selected as $256 \times 256 \times 103$ and $200 \times 200 \times 80$, respectively. Fig.3 shows the three images.

Real HSIs are usually polluted by complex noise. To simulated the various noise distribution in the real scene, four types of noise are added to the original HSI data:

Case 1: Gaussian noise with the same distribution is added to each band of the three simulated datasets, whose mean is 0 and the noise variance σ is set to 0.1.

Case 2: Gaussian noise with different intensity is added to each band of the three simulated datasets, whose mean is 0 and the range of noise variance σ is [0.1,0.2].

Case 3: Gaussian noise the same as Case 2 is added to each band of the three simulated datasets. Besides, 20 bands are chosen randomly to add impulse noise with a percentage of 20%.

Case 4: Gaussian noise and impulse noise the same as Case 3 are added to the original image. We select 10 bands from the impulse noise bands and the other 10 bands from the rest to add deadlines width of 1-3.

1) *Quantitative comparison* : In this paper, four quantitative evaluation indexes are used to measure denoising performance: Mean peak signal-to-noise ratio (MPSNR), which is the average value of PSNR over all bands. PSNR evaluates the similarity between the clean image and denoising image by calculating the mean square error (MSE). Mean structural similarity (MSSIM), which is the average value of SSIM over all bands. SSIM is an evaluation index that measures the structural consistency of images before and after denoising. The erreur relative globale adimensionnelle de synthèse (ERGAS) is a global statistical measure based on the weighted sum of the mean square errors of each band. In addition, mean spectral angle mapping (MSAM) calculates the average of the spectral angles, which represents the similarity between spectra. Among them, higher MPSNR and MSSIM and lower ERGAS and MSA suggest better denoising results.

Table I shows the experimental results of the proposed algorithm and the comparison algorithms on the three datasets, including the values of different evaluation indicators in the four simulated noise situations Case 1-4. The best results are in bold. The denoising results of SWLRTR listed in the last column are bolded except the MSA measure of PaviaU in Case 4, which indicates the proposed method combining weighted low-rank tensor and subspace representation achieves competitive performance compared with other algorithms under the four quantitative index. In order to further demonstrate the denoising effect in each band, Fig.4 and 5 display the PSNR and SSIM value in all bands under four kinds of simulated noises on Pavia University and Pavia Center datasets, where the red line represents the SWLRTR. It can be seen that the red line is higher than others in most bands and cases. Thus, the superiority of this method is verified quantitatively.

2) *Visual comparison* : Fig.6 and Fig.7 show the original image, analog noise image, and the denoising results of different methods to compare the denoising performance of

TABLE I
QUANTITATIVE EVALUATION OF DIFFERENT METHODS ON THE SIMULATED DATA IN DIFFERENT CASES

Data	Noise case	Metrics	Noisy	LRMR	LRTV	LRTDTV	NMoG	L1HyMixDe	SDeCNN	SNLRSF	3DLogTNN	SWLRTR
WDC	Case 1	MPSNR	20.0003	34.2396	31.0162	35.1201	35.8342	35.8338	35.4117	38.3837	35.8497	38.5452
		MSSIM	0.4218	0.9384	0.8689	0.9551	0.9563	0.9525	0.9547	0.9774	0.9641	0.9791
		ERGAS	388.501	72.84	106.019	66.601	61.229	60.546	64.993	45.8951	60.519	45.019
		MSA	0.461	0.092	0.086	0.065	0.071	0.069	0.077	0.0503	0.062	0.049
	Case 2	MPSNR	16.6878	31.5429	29.2826	34.0946	33.7798	33.6042	33.1842	36.7837	34.1315	36.9951
		MSSIM	0.2851	0.895	0.8093	0.9404	0.9315	0.9214	0.9274	0.9671	0.9466	0.97
		ERGAS	586.274	99.492	129.256	74.092	76.933	77.918	83.312	54.4514	73.262	53.131
		MSA	0.633	0.127	0.104	0.077	0.09	0.088	0.096	0.0581	0.074	0.055
	Case 3	MPSNR	16.0763	31.2493	29.1227	32.1896	33.4951	33.145	30.9073	36.2763	33.9541	36.5271
		MSSIM	0.2696	0.8897	0.8033	0.9177	0.9252	0.9145	0.8848	0.9636	0.9444	0.9669
		ERGAS	683.055	102.958	131.649	111.133	79.706	82.643	136.536	57.4614	74.84	55.805
		MSA	0.673	0.132	0.105	0.127	0.094	0.095	0.163	0.0603	0.075	0.057
Case 4	MPSNR	15.9527	31.0065	29.154	31.2589	32.5444	33.0966	29.9408	36.2179	32.1136	36.3291	
	MSSIM	0.2672	0.8857	0.8055	0.9052	0.9136	0.9134	0.8612	0.9633	0.9256	0.966	
	ERGAS	711.236	110.402	131.051	163.731	229.482	85.213	194.206	58.0860	178.079	58.158	
	MSA	0.682	0.14	0.105	0.174	0.211	0.1	0.214	0.0617	0.176	0.061	
PaviaU	Case 1	MPSNR	20.0002	32.8386	32.3885	33.5039	34.4763	34.8787	36.4965	37.4480	34.6318	37.8838
		MSSIM	0.3226	0.8728	0.8841	0.9031	0.9061	0.9178	0.9431	0.9546	0.9301	0.9595
		ERGAS	396.159	91.374	94.852	83.616	77.075	72.405	60.934	55.4246	74.662	52.634
		MSA	0.527	0.129	0.091	0.093	0.1	0.089	0.079	0.0684	0.079	0.065
	Case 2	MPSNR	16.8769	30.3415	30.7691	32.13	32.5218	33.0366	34.4312	35.9842	33.2557	36.5373
		MSSIM	0.2124	0.7983	0.8449	0.8663	0.8626	0.8834	0.9163	0.9397	0.9001	0.9484
		ERGAS	589.422	121.27	113.664	101.972	94.846	88.362	76.217	64.2431	86.487	60.25
		MSA	0.697	0.168	0.101	0.127	0.118	0.105	0.096	0.0759	0.091	0.07
	Case 3	MPSNR	15.3987	29.6441	29.9775	29.2625	31.7338	32.0287	29.3647	34.4958	32.6137	35.2146
		MSSIM	0.1742	0.7757	0.828	0.7866	0.8438	0.8562	0.8137	0.9243	0.8825	0.937
		ERGAS	746.995	130.955	124.891	194.806	102.836	98.805	195.675	75.8599	93.171	70.273
		MSA	0.768	0.172	0.11	0.238	0.125	0.115	0.234	0.085	0.102	0.08
Case 4	MPSNR	15.2812	29.2353	29.1979	28.192	31.6299	32.1282	28.6306	33.8297	29.8944	34.3585	
	MSSIM	0.1801	0.7742	0.8113	0.7674	0.8456	0.8617	0.7837	0.916	0.8454	0.9282	
	ERGAS	790.317	151.634	160.176	272.168	115.189	100.156	266.319	89.4595	257.499	82.77	
	MSA	0.774	0.192	0.176	0.301	0.15	0.119	0.295	0.1042	0.268	0.098	
PaviaC	Case 1	MPSNR	19.9985	32.5801	33.1567	34.0404	34.6891	34.9898	36.0434	37.4129	34.8657	37.6764
		MSSIM	0.436	0.9197	0.9239	0.94	0.9482	0.951	0.9618	0.9726	0.9579	0.9744
		ERGAS	368.977	87.532	80.318	72.838	69.398	65.703	58.248	49.6967	68.15	48.199
		MSA	0.549	0.164	0.081	0.115	0.113	0.103	0.088	0.0688	0.082	0.069
	Case 2	MPSNR	16.8626	29.9801	31.311	32.251	32.4967	32.8791	33.7069	35.6506	33.1611	35.9845
		MSSIM	0.2959	0.864	0.8882	0.8997	0.9207	0.9243	0.9366	0.9598	0.9389	0.9631
		ERGAS	553.476	119.532	99.474	103.478	88.999	83.816	76.676	60.8950	82.633	58.738
		MSA	0.705	0.216	0.092	0.178	0.138	0.125	0.108	0.0787	0.095	0.074
	Case 3	MPSNR	15.4409	29.3152	29.8296	28.4451	31.6063	32.4358	28.1541	33.0666	32.5788	33.9795
		MSSIM	0.2477	0.8456	0.8564	0.8011	0.9066	0.9172	0.8297	0.9236	0.9304	0.9432
		ERGAS	716.014	130.482	167.091	225.046	106.95	88.382	209.581	105.1341	88.584	78.871
		MSA	0.757	0.199	0.208	0.293	0.148	0.121	0.251	0.1579	0.103	0.109
Case 4	MPSNR	14.7497	28.0716	29.711	27.3758	30.5504	31.5816	26.1214	32.2624	28.7468	32.7317	
	MSSIM	0.2344	0.8298	0.853	0.7872	0.8882	0.9085	0.7854	0.9158	0.8859	0.9329	
	ERGAS	789.787	191.133	190.804	315.467	218.072	103.195	282.831	121.3199	286.35	92.804	
	MSA	0.784	0.256	0.205	0.356	0.25	0.131	0.315	0.1682	0.304	0.121	

TABLE II
CLASSIFICATION RESULTS ON KENNEDY SPACE CENTER(KSC) DATASET WITH DIFFERENT DENOISING METHODS

Class	Noisy	LRMR	LRTV	LRTDTV	NMoG	L1HyMixDe	SDeCNN	SNLRSF	3DLogTNN	SWLRTR
Scrub	0.8333	0.8333	0.9868	0.9481	1	0.9481	1	1	1	1
Willow swamp	0.7667	0.7667	1	0.8571	0.8846	1	0.8889	1	1	1
CP hammock	0.697	0.6098	0.9615	0.7826	0.8621	1	1	0.8571	0.96	0.9615
CP/Oak	0.3929	1	0.7667	0.5313	0.697	0.84	1	0.84	0.6765	1
Slash pine	0.8000	1	0.8333	0.6667	0.8182	0.6667	0.8421	0.8571	0.75	1
Oak/Broadleaf	0.6667	0.6923	0.9524	0.5789	0.85	0.7826	1	0.8462	0.9167	0.9200
Hardwood swamp	1.0000	0.9167	1	0.9091	0.9091	0.9167	1.0000	1	1	1
Graminoid marsh	0.7778	0.8205	1	0.7857	0.9286	0.9762	0.9545	0.9091	0.9762	1
Spartina marsh	0.8276	0.8276	0.963	0.8070	0.963	0.9455	0.9808	0.9808	0.9455	0.9811
Catiail marsh	1	1	1	0.8043	1	1	1	1	1	1
Salt marsh	1	1	1	0.9737	1	1	1	1	1	1
Mud flats	0.8103	0.8909	1	0.8333	0.9796	1	1	1	1	1
Water	1	1	1	0.9783	1	1	1	1	1	1
OA	0.8429	0.8755	0.9732	0.8467	0.9444	0.9559	0.9828	0.9636	0.9617	0.9923
AA	0.8132	0.8737	0.9587	0.8043	0.9148	0.9289	0.9743	0.9454	0.9404	0.9894
Kappa	0.8247	0.8611	0.9701	0.8293	0.9382	0.9509	0.9808	0.9595	0.9574	0.9915

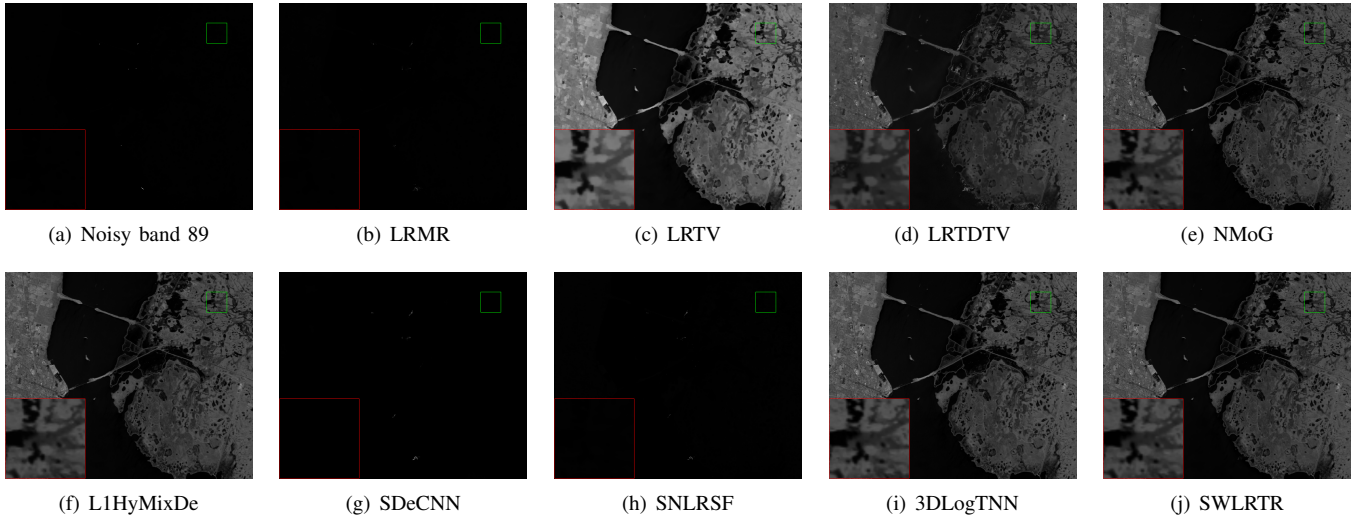


Fig. 9. Denoising results for KSC dataset.

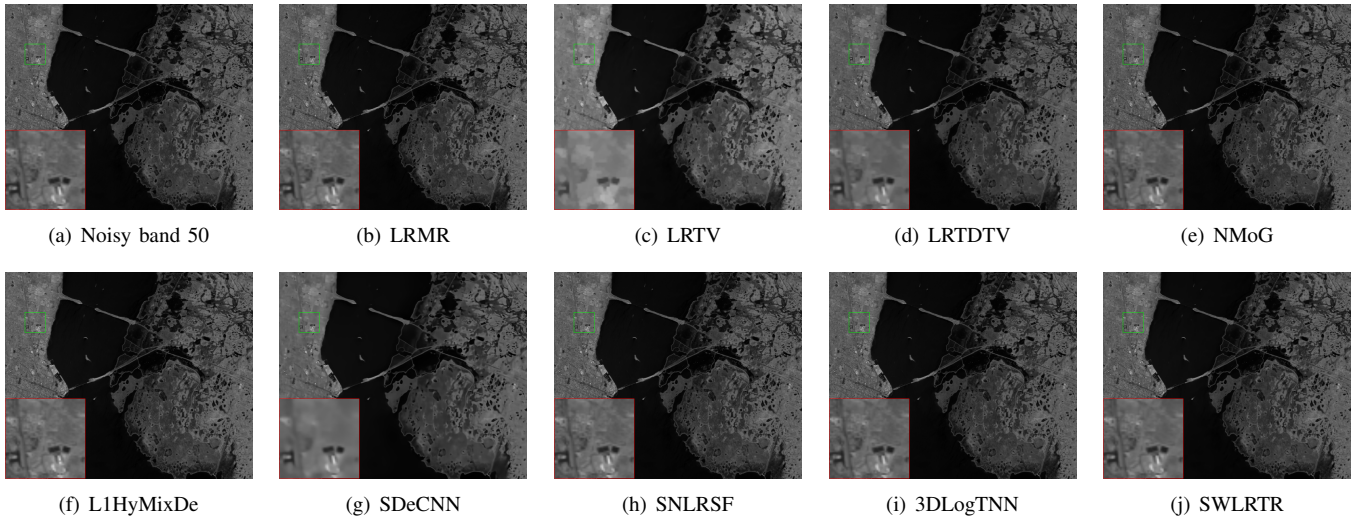


Fig. 10. Denoising results for KSC dataset.

TABLE III
RUNNING TIME OF DIFFERENT DENOISING METHODS ON THE THREE SIMULATED DATA

Dataset	LRMR	LRTV	LRTDTV	NMoG	L1HyMixDe	SDeCNN	SNLRSF	3DLogTNN	SWLRTR
WDC	48	46	154	144	234	60	400	442	70
PaviaU	34	33	85	104	244	33	407	189	69
PaviaC	19	18	43	53	147	14	243	77	14

different methods visually. Specifically, on the PaviaU dataset in Fig.6, band 60 is selected as a representative band because it includes Gaussian noise and impulse noise. Fig.7 show the recovery results in band 64 destroyed by Gaussian noise, impulse noise, and deadlines on PaviaC dataset. It can be seen that the SWLRTR retains the details and removes the unexpected mixed noise well compared with other algorithms in Fig.6(c)-(k). LRM, L1HyMixDe, SDeCNN, and 3DLogTNN are difficult to eliminate the deadlines in Fig.7(c,g,h,j), and even cause a certain degree of degradation when dealing with strong noise. The denoised images obtained by LRTDTV and SNLRSF are oversmooth, some details in the original image

are lost, and the edges of graphics become blurred in Fig.7(e,i). NMoG introduces various levels of artifacts to the denoised image and blurring some details in Fig.7(f). Therefore, the capability in removing mixed noise of the SWLRTR is proved from a visual perspective.

3) *Running time* : Table III demonstrates the improvement of the proposed method in terms of computational complexity indicating the average computational time (second) of different methods for the three simulated datasets. The fastest results are highlighted in bold. The proposed SWLRTR has the shortest implementation time on the PaviaC dataset. On the other two datasets, SWLRTR is slower than LRM, LRTV, and

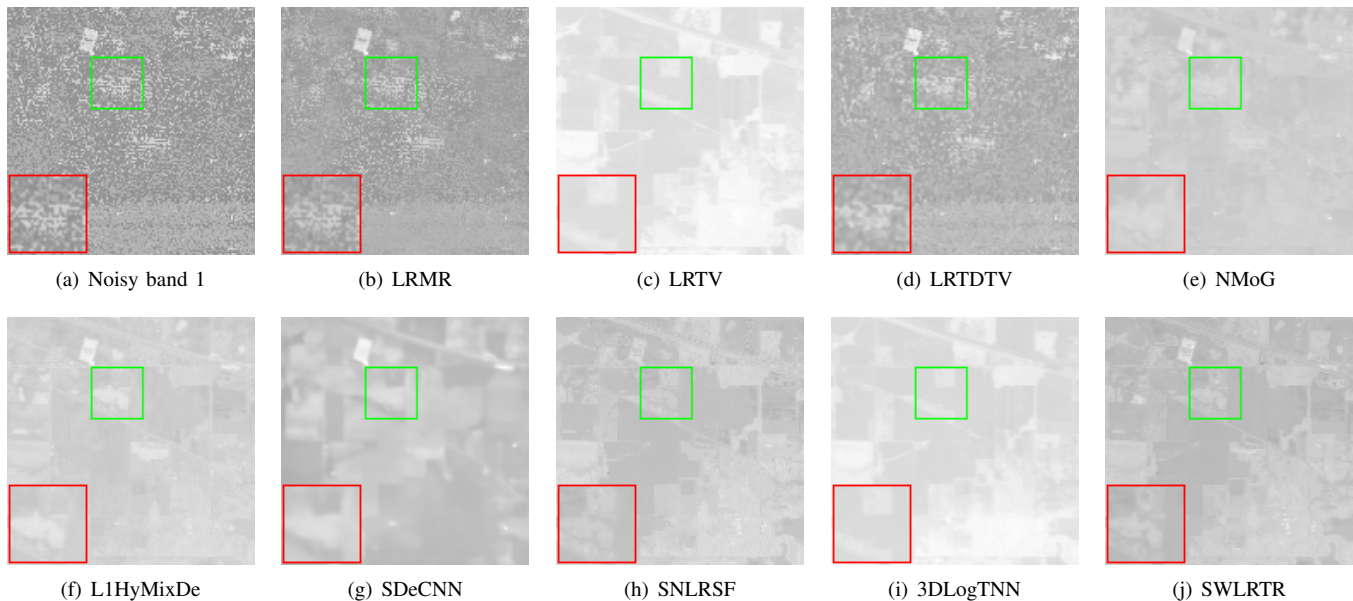


Fig. 11. Denoising results for Indian Pines dataset.

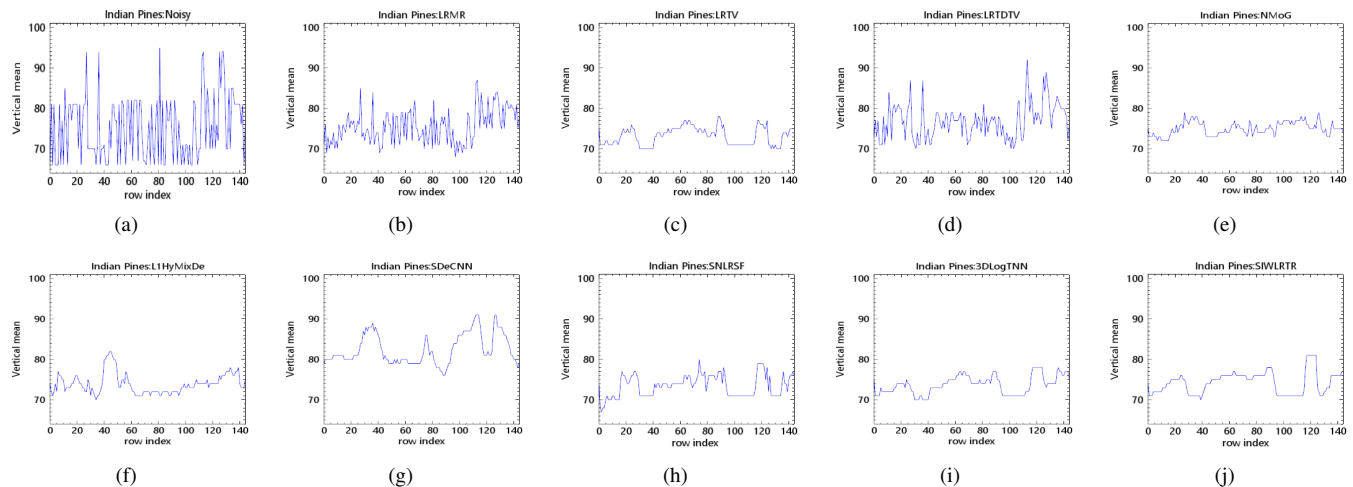


Fig. 12. Vertical mean profiles of band 28 in the real Indian Pines dataset experiment.

SDeCNN. The proposed method has low complexity while ensuring denoising performance.

B. Real data experiment

In this section, we design real datasets experiments to prove the effectiveness of the SWLRTR on real-world noise. The Kennedy Space Center (KSC) dataset is size of $512 \times 614 \times 176$ after removing bands with poor quality. The Indian Pines dataset includes 145×145 pixels and 224 spectral bands. The two hyperspectral images are presented in Fig.8. The aforementioned two datasets are employed in our real data experiments.

1) *KSC dataset* : Due to the real dataset has no ground truth image as reference, we use the classification results provided by the radial basis function (RBF) kernel support vector machine to evaluate the performance of SWLRTR on the real dataset quantitatively. The KSC dataset contains 13

different types of land coverings that occur in the environment. Three evaluation indicators are listed in Table II namely the accuracy of each class, overall accuracy (OA), average accuracy (AA), and Kappa statistic. The best results are in bold. We can observe the proposed SWLRTR achieves the best results in all three measures compared with other methods which indicating the effectiveness in real image denoising. The denoising results on bands 89 and 50 are represented in Fig.9 and 10, respectively. From the figures, LRMR, SDeCNN, and SNLRSF can not restore the image well (Fig.9), LRTV causes the image to be oversmooth, LRTDTV, NMoG L1HyMixDe, and 3DLogTNN tend to weaken the edges and details (Fig.10).

2) *Indian Pines dataset* : In the Indian Pines dataset, we show the restored HSIs of band 1 recovered by all competing methods in Fig.11 as an instance, because band 1 includes obvious impulse noise and other unknown noise. From Fig.11(b,d), we can see LRMR and LRTDTV do not

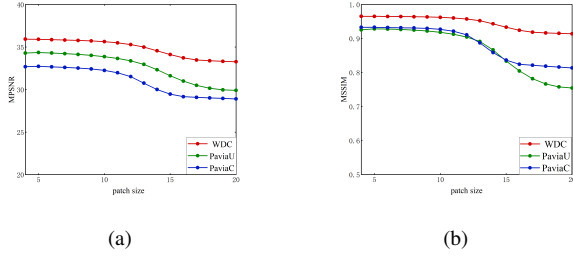


Fig. 13. Sensitivity analysis of patch size

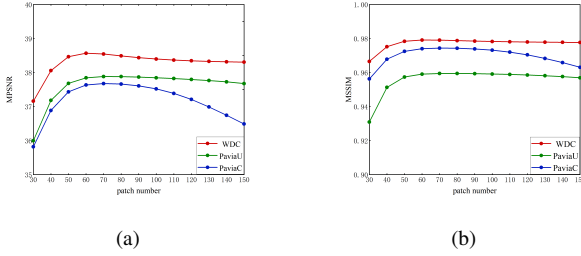


Fig. 14. Sensitivity analysis of patch number

remove the impulse noise completely; LRTV, L1HyMixDe, and 3DLogTNN introduce the spectral distortion artifact; the result of NMoG is oversmooth; SDeCNN and SNLRSF have better performance than NMoG, however, still miss lots of details; as for the result of SWLRTR, the noise is removed satisfactorily and the different structural edges are preserved well. The validity of the proposed method is further proved by vertical mean profiles of band 28 in Fig.12. The profiles are drawn according to the mean value of pixels in each column. Due to the presence of noise, the curve in the figure shows rapid fluctuations before denoising, and the fluctuations are suppressed by different methods after the restoration processing. From Fig.12 (j), the curve of SWLRTR method is smoother than others, which follows the visual results presented in Fig.11.

C. Sensitivity analysis

The proposed SWLRTR contains five important parameters, including patch size p , the number of similar patches q , subspace dimension k , and regularized parameters λ_1, λ_2 . In this section, we experimentally explore the optimal settings of

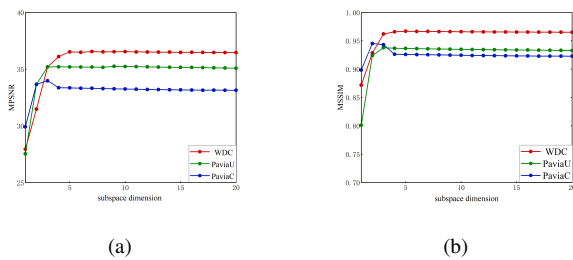


Fig. 15. Sensitivity analysis of subspace dimension

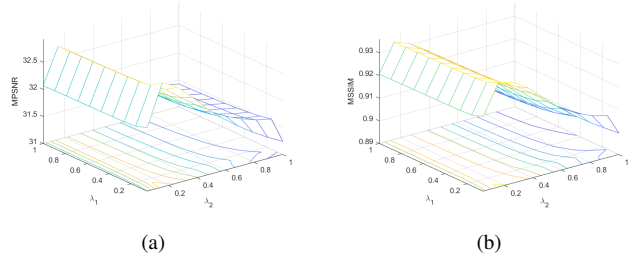


Fig. 16. Sensitivity analysis of regularization parameters λ_1 and λ_2

these parameters. Besides, the experiments are implemented in the simulated datasets of case 4.

1) *patch size p* : By changing p from 3 to 20, Fig.13 shows the denoising results of MPSNR and MSSIM. The step size is set to 3. As we can see, the denoising results are relatively stable for $3 < p < 10$, then appears degradation when $p > 10$. When the selected patch is too small, the local spatial information within the image will be lost and not conducive to block matching, when the selected patch is too large, the detail information will be eliminated. In addition, with the increase of patch size, the amount of calculation will also increase. In order to have better denoising ability and lower computational complexity, the patch size is set to 5 in our experiments.

2) *the number of similar patches q* : The number of similar patches selected in the block matching stage is also an important parameter that affects the results of image denoising. In the sensitivity experiment, the parameter q is selected from 30 to 150. Fig.14 presents the corresponding MPSNR and MSSIM values where the highest MPSNR and MSSIM are achieved at $50 < q < 70$ for different datasets. The main reason is that either too large or too small number of similar patches can lead to insufficient use of nonlocal self-similarity. Hence, we choose the similar patch number q according to the noise intensity, fewer patches are selected when the noise is heavy, vice versa. In this paper, q is set to 70 when the noise variance less than or equal to 0.1, otherwise, q is set to 70.

3) *subspace dimension k* : Generally, the optimal subspace dimension is distinct for different datasets. The proposed method achieves the best denoising result when the subspace dimension is 5, 4, 3 for WDC, PaviaU, and PaviaC dataset, respectively, as presented in Fig.15. In the real data experiment, the subspace dimension is set to 10, 25 for KSC and Indian Pines dataset. Besides, the subspace dimension is manually adjusted in our experiments, which is usually different from the value obtained by the HySime algorithm, because the algorithm only considers Gaussian noise leading to an inaccurate estimate.

4) *regularized parameter λ_1, λ_2* : By varying λ_1 and λ_2 from 0 to 1 with a step size of 0.05, Fig.16 shows the denoising results under MPSNR and MSSIM measurements. Therefore, in order to achieve robust performance, the parameter λ_1 and λ_2 are set to 0.2, 0.1, respectively.

VI. CONCLUSION

In this paper, a novel hyperspectral image denoising model integrated the weighted low-rank tensor regularization term

and subspace representation for mixed noise is proposed. Based on the fact that HSI exists in multiple subspaces, each spectral signature can be represented by a linear combination of a few pure spectral endmembers. The global spectral low rankness can be enforced by decomposing the HSI into mode-3 tensor-matrix product of a reduced image and a low-dimensional orthogonal matrix. The experimental results show that the computational cost is greatly reduced because of the subspace representation. To further utilize the priors in HSI, a low-rank tensor is constructed by aggregating the similar patches searched from the reduced image, then we introduce the weighted low-rank tensor regularizer to exploit its low rankness. Specifically, the regularization punishes the elements in the core tensor reasonably. Besides, we design an algorithm for solving the model based on alternate minimization. Experiments on simulated and real datasets show that the proposed algorithm has better denoising performance compared with other advanced algorithms.

REFERENCES

- [1] G. Lu and B. Fei, "Medical hyperspectral imaging: a review," *Journal of Biomedical Optics*, vol. 19, no. 1, p. 10901, 2014.
- [2] D. G. Ferris, R. A. Lawhead, E. D. Dickman, N. Holtzapfle, J. A. Miller, S. Grogan, S. Bambot, A. Agrawal, and M. L. Faupel, "Multimodal hyperspectral imaging for the noninvasive diagnosis of cervical neoplasia," *Journal of Lower Genital Tract Disease*, vol. 5, no. 2, 2001.
- [3] G. Mooradian, M. Weiderhold, A. E. Dabiri, and C. Coyle, "Hyperspectral imaging methods and apparatus for non-invasive diagnosis of tissue for cancer," 1998.
- [4] B. A. Martini and T. D. Cocks, "Operational airborne hyperspectral remote sensing for global geothermal exploration," in *IEEE International Geoscience & Remote Sensing Symposium*, 2004, pp. 625–626.
- [5] C. Kratt, W. Calvin, and M. Coolbaugh, "Geothermal exploration with hynmap hyperspectral data at brady-desert peak, nevada," *Remote Sensing of Environment*, vol. 104, no. 3, pp. 313–324, 2006.
- [6] K. A. Reath and M. S. Ramsey, "Exploration of geothermal systems using hyperspectral thermal infrared remote sensing," *Journal of Volcanology & Geothermal Research*, vol. 265, no. sep.1, pp. 27–38, 2013.
- [7] H. Erives and G. J. Fitzgerald, "Automated registration of hyperspectral images," in *Conference on Remote Sensing and Modeling of Ecosystems for Sustainability; 2004/0802-04; Denver, CO (US)*, 2004.
- [8] M. Teke, H. S. Deveci, O. Haliloğlu, S. Gürbüz, and U. Sakarya, "A short survey of hyperspectral remote sensing applications in agriculture," in *International Conference on Recent Advances in Space Technologies*, 2013.
- [9] P. Stefano, P. Angelo, P. Simone, R. Filomena, S. Federico, S. Tiziana, A. Umberto, C. Vincenzo, N. Acito, and D. Marco, "The prisma hyperspectral mission: Science activities and opportunities for agriculture and land monitoring," *IEEE*, 2014.
- [10] G. Camps-Valls and L. Bruzzone, "Kernel-based methods for hyperspectral image classification," *IEEE Transactions on Geoscience & Remote Sensing*, vol. 43, no. 6, pp. 1351–1362, 2005.
- [11] J. A. Benediktsson, J. A. Palmason, and J. R. Sveinsson, "Classification of hyperspectral data from urban areas based on extended morphological profiles," *IEEE Transactions on Geoscience & Remote Sensing*, vol. 43, no. 3, pp. 480–491, 2005.
- [12] D. Manolakis, C. Siracusa, and G. Shaw, "Hyperspectral subpixel target detection using the linear mixing model," *Geoscience & Remote Sensing IEEE Transactions on*, vol. 39, no. 7, pp. 1392–1409, 2001.
- [13] S. S. Chiang, C. I. Chang, and I. W. Ginsberg, "Unsupervised target detection in hyperspectral images using projection pursuit," *Geoscience & Remote Sensing IEEE Transactions on*, vol. 39, no. 7, pp. 1380–1391, 2001.
- [14] H. Othman and S. E. Qian, "Noise reduction of hyperspectral imagery using hybrid spatial-spectral derivative-domain wavelet shrinkage," *IEEE Transactions on Geoscience & Remote Sensing*, vol. 44, no. 2, pp. 397–408, 2006.
- [15] Y. Qian and M. Ye, "Hyperspectral imagery restoration using nonlocal spectral-spatial structured sparse representation with noise estimation," *IEEE Journal of Selected Topics in Applied Earth Observations & Remote Sensing*, vol. 6, no. 2, pp. 499–515, 2013.
- [16] P. Zhong and R. Wang, "Multiple-spectral-band crfs for denoising junk bands of hyperspectral imagery," *IEEE TRANSACTIONS ON GEOSCIENCE AND REMOTE SENSING*, 2013.
- [17] Q. Yuan, L. Zhang, and H. Shen, "Hyperspectral image denoising employing a spectral-spatial adaptive total variation model," *IEEE Transactions on Geoscience and Remote Sensing*, vol. 50, no. 10, pp. 3660–3677, 2012.
- [18] G. Y. Chen and W. P. Zhu, "Signal denoising using neighbouring dual-tree complex wavelet coefficients," in *Conference on Electrical & Computer Engineering*, 2009.
- [19] B. Rasti, J. R. Sveinsson, and M. O. Ulfarsson, "Wavelet-based sparse reduced-rank regression for hyperspectral image restoration," *IEEE Transactions on Geoscience & Remote Sensing*, vol. 52, no. 10, pp. 6688–6698, 2014.
- [20] T. Lu, S. Li, L. Fang, Y. Ma, and J. A. Benediktsson, "Spectral-spatial adaptive sparse representation for hyperspectral image denoising," *IEEE Trans. Geosci. Remote. Sens.*, vol. 54, no. 1, pp. 373–385, 2016. [Online]. Available: <https://doi.org/10.1109/TGRS.2015.2457614>
- [21] H. Zhang, H. Wei, L. Zhang, H. Shen, and Q. Yuan, "Hyperspectral image restoration using low-rank matrix recovery," *IEEE Transactions on Geoscience and Remote Sensing*, vol. 52, no. 8, pp. 4729–4743, 2014.
- [22] E. J. Candès, X. Li, Y. Ma, and J. Wright, "Robust principal component analysis?" *CoRR*, vol. abs/0912.3599, 2009. [Online]. Available: <http://arxiv.org/abs/0912.3599>
- [23] W. He, H. Zhang, L. Zhang, and H. Shen, "Hyperspectral image denoising via noise-adjusted iterative low-rank matrix approximation," *IEEE Journal of Selected Topics in Applied Earth Observations and Remote Sensing*, vol. 8, no. 6, pp. 1–12, 2015.
- [24] Y. Chen, Y. Guo, Y. Wang, W. Dong, P. Chong, and G. He, "Denoising of hyperspectral images using nonconvex low rank matrix approximation," *IEEE Transactions on Geoscience and Remote Sensing*, vol. 55, no. 9, pp. 5366–5380, 2017.
- [25] Y. Xie, Y. Qu, D. Tao, W. Wu, Q. Yuan, and W. Zhang, "Hyperspectral image restoration via iteratively regularized weighted Schatten p-norm minimization," *IEEE Transactions on Geoscience & Remote Sensing*, vol. 54, no. 8, pp. 4642–4659, 2016.
- [26] W. He, H. Zhang, L. Zhang, and H. Shen, "Total-variation-regularized low-rank matrix factorization for hyperspectral image restoration," *IEEE Transactions on Geoscience & Remote Sensing*, vol. 54, no. 1, pp. 178–188, 2015.
- [27] M. Wang, Y. Jing, J. H. Xue, and W. Sun, "Denoising of hyperspectral images using group low-rank representation," *IEEE Journal of Selected Topics in Applied Earth Observations & Remote Sensing*, vol. 9, no. 9, pp. 4420–4427, 2016.
- [28] J. Xue, Y. Zhao, W. Liao, and S. G. Kong, "Joint spatial and spectral low-rank regularization for hyperspectral image denoising," *IEEE Transactions on Geoscience & Remote Sensing*, vol. 56, no. 99, pp. 1940–1958, 2018.
- [29] X. Liu, S. Bourennane, and C. Fossati, "Denoising of hyperspectral images using the parafac model and statistical performance analysis," *IEEE Transactions on Geoscience & Remote Sensing*, vol. 50, no. 10, pp. 3717–3724, 2012.
- [30] X. Qi, Z. Qian, D. Meng, Z. Xu, and S. Gu, "Multispectral images denoising by intrinsic tensor sparsity regularization," in *IEEE Conference on Computer Vision & Pattern Recognition*, 2016.
- [31] Y. Chang, L. Yan, H. Fang, S. Zhong, and Z. Zhang, "Weighted low-rank tensor recovery for hyperspectral image restoration," *arXiv*, 2017.
- [32] Haiyan, Fan, Yunjin, Chen, Yulan, Guo, Hongyan, Zhang, Gangyao, and Kuang, "Hyperspectral image restoration using low-rank tensor recovery," *IEEE Journal of Selected Topics in Applied Earth Observations and Remote Sensing*, vol. 10, no. 10, pp. 4589–4604, 2017.
- [33] Y. Wang, J. Peng, Q. Zhao, Y. Leung, X. L. Zhao, and D. Meng, "Hyperspectral image restoration via total variation regularized low-rank tensor decomposition," *IEEE Journal of Selected Topics in Applied Earth Observations and Remote Sensing*, 2017.
- [34] H. Fan, L. Chang, Y. Guo, G. Kuang, and J. Ma, "Spatial-spectral total variation regularized low-rank tensor decomposition for hyperspectral image denoising," *IEEE Transactions on Geoscience and Remote Sensing*, vol. PP, no. 99, pp. 1–18, 2018.
- [35] C. Yi, L. Yan, and Z. Sheng, "Hyper-laplacian regularized unidirectional low-rank tensor recovery for multispectral image denoising," in *2017 IEEE Conference on Computer Vision and Pattern Recognition (CVPR)*, 2017.

- [36] Bioucas-Dias, M. J., Nascimento, and J. M. P., "Hyperspectral subspace identification," *Geoscience & Remote Sensing IEEE Transactions on*, 2008.
- [37] L. Zhuang and J. M. Bioucas-Dias, "Hyperspectral image denoising based on global and non-local low-rank factorizations," in *2017 IEEE International Conference on Image Processing (ICIP)*, 2018.
- [38] Zhuang, L. and Bioucas-Dias, J. M. , "Fast hyperspectral image denoising and inpainting based on low-rank and sparse representations," *IEEE Journal of Selected Topics in Applied Earth Observations & Remote Sensing*, vol. 11, no. 99, pp. 730–742, 2018.
- [39] L. Sun, B. Jeon, B. N. Soomro, Y. Zheng, Z. Wu, and L. Xiao, "Fast superpixel based subspace low rank learning method for hyperspectral denoising," *IEEE Access*, vol. 6, pp. 1–1, 2018.
- [40] W. He, Q. Yao, C. Li, N. Yokoya, and Q. Zhao, "Non-local meets global: An integrated paradigm for hyperspectral denoising," in *2019 IEEE/CVF Conference on Computer Vision and Pattern Recognition (CVPR)*, 2019.
- [41] C. Cao, J. Yu, C. Zhou, K. Hu, F. Xiao, and X. Gao, "Hyperspectral image denoising via subspace-based nonlocal low-rank and sparse factorization," *IEEE J. Sel. Top. Appl. Earth Obs. Remote. Sens.*, vol. 12, no. 3, pp. 973–988, 2019. [Online]. Available: <https://doi.org/10.1109/JSTARS.2019.2896031>
- [42] W. He, Q. Yao, C. Li, N. Yokoya, and Q. Zhao, "Non-local meets global: An integrated paradigm for hyperspectral denoising," in *2019 IEEE/CVF Conference on Computer Vision and Pattern Recognition (CVPR)*, 2019, pp. 6861–6870.
- [43] L. Zhuang and M. K. Ng, "Hyperspectral mixed noise removal by 11-norm based subspace representation," *IEEE Journal of Selected Topics in Applied Earth Observations and Remote Sensing*, vol. PP, no. 99, pp. 1–1, 2020.
- [44] A. Maffei, J. M. Haut, M. E. Paoletti, J. Plaza, L. Bruzzone, and A. Plaza, "A single model cnn for hyperspectral image denoising," *IEEE Transactions on Geoscience and Remote Sensing*, vol. 58, no. 4, pp. 2516–2529, 2020.
- [45] Y. B. Zheng, T. Z. Huang, X. L. Zhao, T. X. Jiang, and T. Y. Ji, "Mixed noise removal in hyperspectral image via low-fibered-rank regularization," *IEEE Transactions on Geoscience and Remote Sensing*, vol. PP, no. 99, pp. 1–16, 2019.